research papers

Versatile compact heater design for *in situ* nano-tomography by transmission X-ray microscopy

Stephen Antonelli,[a] Arthur Ronne,[b] Insung Han,[c] Mingyuan Ge,[a] Bobby Layne,[d] Ashwin J. Shahani,[c] Kazuhiro Iwamatsu,[d] James F. Wishart,[d] Steven L. Hulbert,[a] Wah-Keat Lee,[a] Yu-chen Karen Chen-Wiegart[b,a]* and Xianghui Xiao[a]*

[a]National Synchrotron Light Source II, Brookhaven National Laboratory, Upton, NY 11973, USA, [b]Department of Materials Science and Chemical Engineering, Stony Brook University, Stony Brook, NY 11794, USA, [c]Department of Materials Science and Engineering, University of Michigan, Ann Arbor, MI 48109, USA, and [d]Chemistry Division, Brookhaven National Laboratory, Upton, NY 11973, USA.
*Correspondence e-mail: karen.chen-wiegart@stonybrook.edu, xiao@bnl.gov

A versatile, compact heater designed at National Synchrotron Light Source-II for *in situ* X-ray nano-imaging in a full-field transmission X-ray microscope is presented. Heater design for nano-imaging is challenging, combining tight spatial constraints with stringent design requirements for the temperature range and stability. Finite-element modeling and analytical calculations were used to determine the heater design parameters. Performance tests demonstrated reliable and stable performance, including maintaining the exterior casing close to room temperature while the heater is operating at above 1100°C, a homogenous heating zone and small temperature fluctuations. Two scientific experiments are presented to demonstrate the heater capabilities: (i) *in situ* 3D nano-tomography including a study of metal dealloying in a liquid molten salt extreme environment, and (ii) a study of pore formation in icosahedral quasicrystals. The progression of structural changes in both studies were clearly resolved in 3D, showing that the new heater enables powerful capabilities to directly visualize and quantify 3D morphological evolution of materials under real conditions by X-ray nano-imaging at elevated temperature during synthesis, fabrication and operation processes. This heater design concept can be applied to other applications where a precise, compact heater design is required.

1. Introduction

Direct visualization and quantification of the 3D morphology of materials under real conditions are crucial for understanding the processing structure–property correlations associated with a wide variety of novel material systems (Gatalo *et al.*, 2019; Topsøe, 2003; Johnson *et al.*, 2019; Li *et al.*, 2015). The reaction rates and materials evolution mechanisms occurring during these real-world processes are highly dependent on the operating temperature, which activates different chemical reactions and physical transport phenomena (Chen-Wiegart, Wang *et al.*, 2012; Voorhees, 1985; Waldmann *et al.*, 2014; Liu *et al.*, 2019; Moniri *et al.*, 2019; Han *et al.*, 2019; Shahani *et al.*, 2016; Gibbs *et al.*, 2015). Therefore, the ability to study these processes at variable and elevated temperatures is critical to a broad range of scientific disciplines utilizing materials.

Recent advances in full-field X-ray nano-imaging with transmission X-ray microscopy (TXM) (Ge *et al.*, 2018; Xu *et al.*, 2017; Zhao *et al.*, 2018; Cheng *et al.*, 2017) have generated unprecedented capabilities to analyze materials at sub-30 nm resolution in 3D. Impactful applications include energy storage (Tsai *et al.*, 2018; Landa-Medrano *et al.*, 2017; Yang *et al.*, 2019), catalysis (Gonzalez-Jimenez *et al.*, 2012), metals and
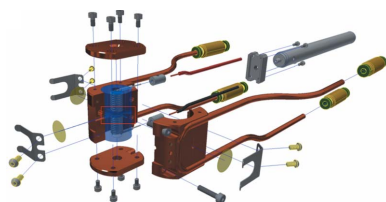
alloys (Kaira *et al.*, 2019; Milhet *et al.*, 2018), high-pressure studies (Mao *et al.*, 2019), and fuel cells (Chen-Wiegart, Harris *et al.*, 2012; Harris *et al.*, 2015; Izzo *et al.*, 2008). Recently, the Full-field X-ray Imaging (FXI) beamline at National Synchrotron Light Source-II (NSLS-II) demonstrated that full nano-tomography images can be performed within 1 min (Ge *et al.*, 2018), enabling dynamical and kinetic studies with much higher temporal and spatial resolutions than previously possible.

To enable *in situ* heating studies with the FXI TXM, and for rapid X-ray nano-imaging more generally, it is important to design a versatile heater that is compact, stable and repeatable. Owing to the short (~11 mm) working distance of the adjacent TXM optics at FXI and the requirement of a stable temperature up to ~1100°C driven by many materials applications, the heater design requires careful consideration of the competing demands. Prior heater design efforts have taken a variety of approaches to tackle similar challenges. For micro-tomography, Fife *et al.* demonstrated a laser-based heater design for *in situ* micro-tomography at the TOMCAT beamline at the Swiss Light Source (Fife *et al.*, 2012), and Bale *et al.* studied sequences of micro-crack damage in ceramic matrix composites under mechanical load at temperatures up to 1750°C using a heater design developed at the Advanced Light Source (Bale *et al.*, 2013; Barnard *et al.*, 2017). For nano-tomography, Kiss *et al.* designed a resistance-based heater to study Ni powder oxidation from 670 to 830°C at a TXM (Kiss *et al.*, 2015). At FXI, the development of a new heater design

is driven by space constraints, the ability to heat a rotating sample for rapid nano-tomography data collection and the capability to reach temperatures up to 1100°C.

In this work, we present a description of the design, analysis and performance for an *in situ* heater for X-ray nano-imaging. We include the results from two scientific-use cases to highlight the heater design versatility: (i) 3D tomography under liquid molten salt extreme environment to study metal corrosion and dealloying, and (ii) rapid 3D tomography to study the formation of extended defects in complex inter-metallics.

2. Furnace design

2.1. Heater design

The heater was designed to be compact and lightweight to comply with the tight spatial constraints of the TXM sample environment and optics. The heater is required to facilitate heating a sample up to ~1100°C while maintaining an outer surface temperature below 40°C. At FXI, the distance between the pinhole and the sample positions is 11 mm, thereby introducing a size constraint in the heater design.

An exploded view of the heater design is shown in Fig. 1. Fig. 1(*a*) depicts the overall structure of the heater and Fig. 1(*b*) shows a zoomed-in view of the heating element. The key part of the heater consists of a ceramic insulated resistive heating coil packaged inside a water-cooled copper casing.
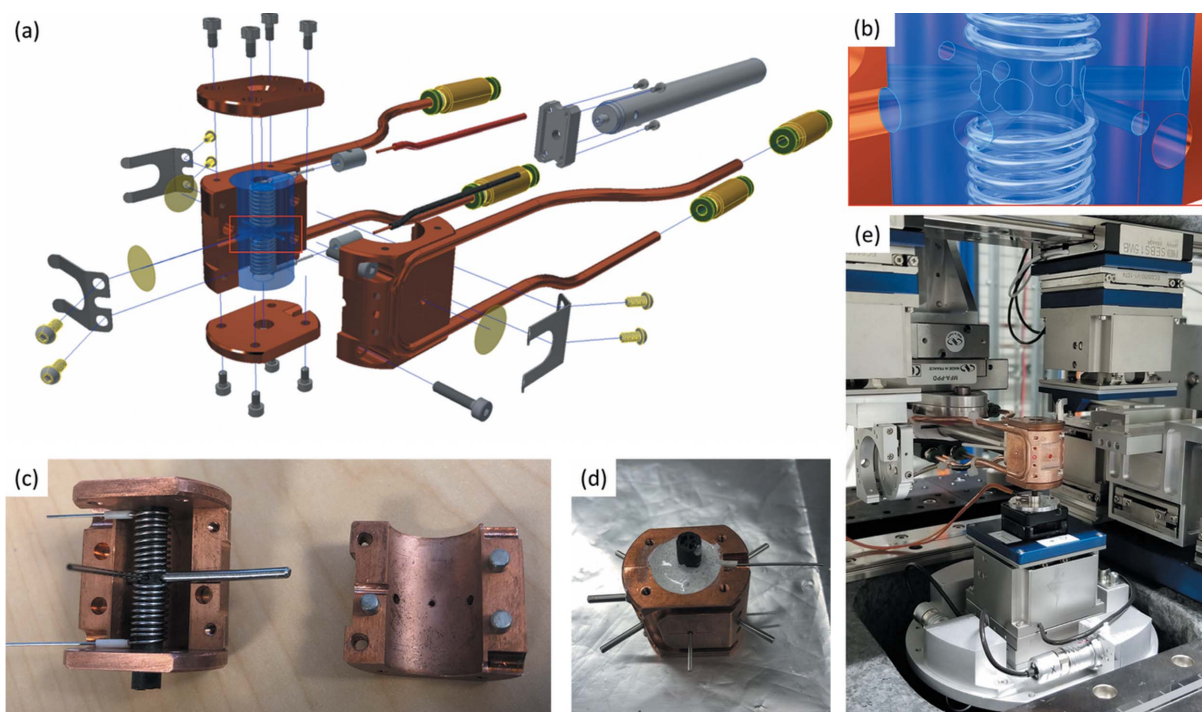

Figure 1
In situ heater assembly. (*a*) Overall structure of the heater. (*b*) Heating element region. The heater is approximately cylindrical in shape. A sample can be mounted at the end of a thin rod holder base then inserted into the heating chamber through the bottom opening. (*c*, *d*) Detailed structure of the core-pin assembly. (*e*) Final entire heater assembly mounted at the FXI beamline at NSLS-II.

The casing design consists of two halves for easy installation of the heater unit inside it. The heater unit is composed of a resistive heater coil made from a continuous segment of Kanthal A-1 wire (22AWG, 0.0253 inch diameter) and a thermally insulating ceramic layer. A special core-pin assembly was designed to help ensure that the coil wire is kept clear of the TXM field of view [Figs. 1(c) and 1(d)]. Assembly of the heater unit was completed by casting ceramic paste (Aremco Ceramacast 510, a castable ceramic) around the core-pin assembly inside a cylindrical mold.

Seven penetrations radially distributed through the casing in the horizontal plane (sample plane) allow passageways for the incoming and outgoing X-ray beams, visual access for the side-facing camera, as well as onboard temperature sensor placement. The heater also includes copper top and bottom caps for enclosing the heater unit inside a cooling environment. Different versions of the top cap, with and without an opening hole, are selectable to accommodate different sample geometries. A pair of U-shape copper cooling pipes were brazed onto the copper casing halves. The heater was machined in-house. The heater assembly was mounted on a motorized stage stack for precise positioning [Fig. 1(e)].

2.2. Finite-element modeling analysis on heater design

A steady-state thermal finite-element model of the heater assembly was constructed to assist in predicting the performance and optimizing operational parameters. Analysis results in Figs. 2(a) and 2(b) show that, while the temperature at the sample position reached ∼1100°C [Fig. 2(a)], the temperature of the copper casing remains less than 40°C [Fig. 2(b)]. For further details on finite element modeling analysis see Section S1 of the supporting information.

2.3. Furnace tests

A K-type thermocouple (A) was used to calibrate the actual temperature at the sample position. The thermocouple was fixed onto the beamline standard kinematic mounting base plate and protruded into the furnace chamber from below. The thermocouple tip was aligned and centered at the TXM field of view. This configuration simulated a generic sample mounting scheme in which a sample would be mounted on top of a thin ceramic rod or thin-walled quartz tube with ceramic wool inside to hold the sample in place. During the
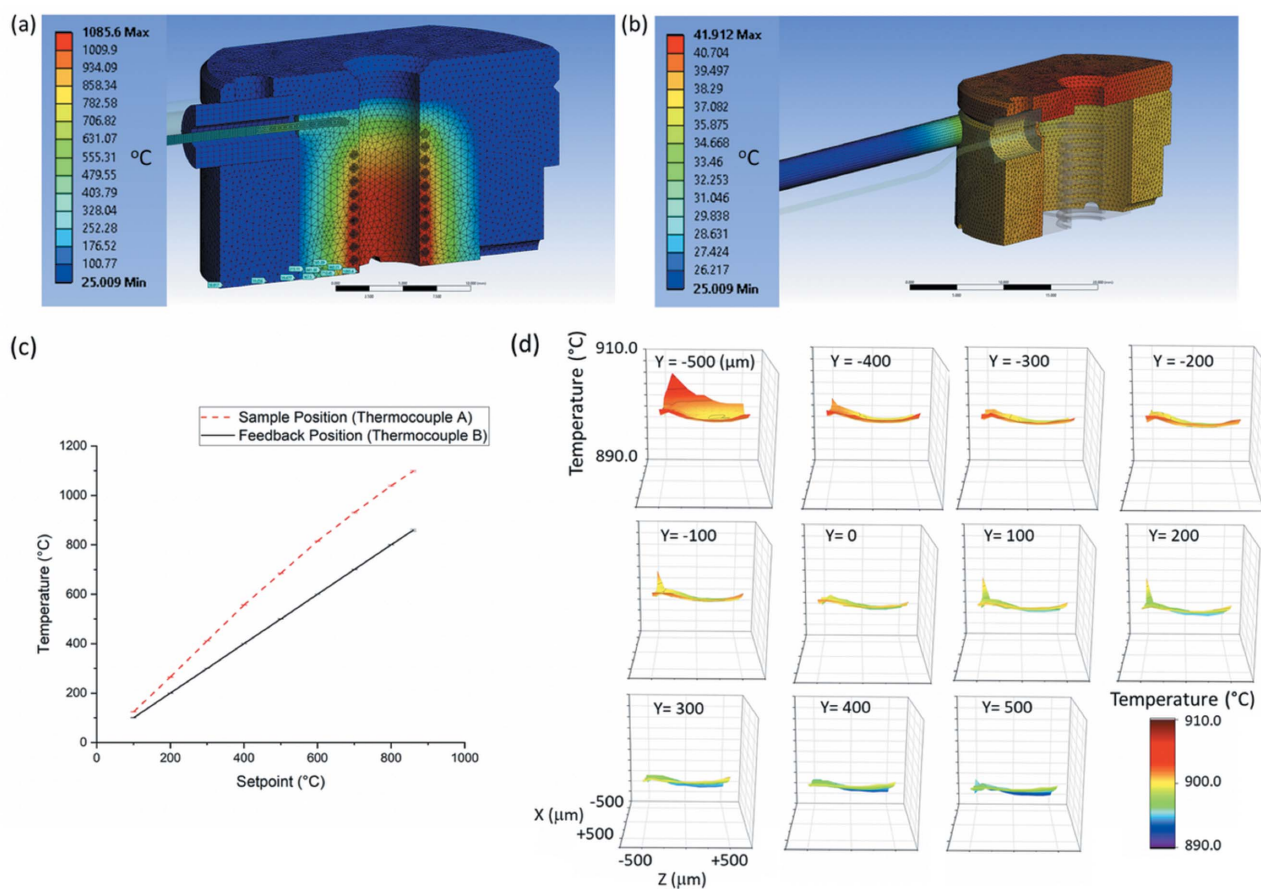

Figure 2
Finite-element analysis: (a) the temperature distribution of the heating element around the sample position can reach 1100°C, and (b) the temperature of the copper casing remains less than 40°C. (c) Temperature calibration curve. The error bars (exaggerated by a factor of 10 for visibility on the graph) are the standard deviation of each segment and indicate the temperature fluctuation. (d) 3D heating zone characterization.

temperature ramping stage, the thermocouple tip moves due to thermal expansion of the thermocouple. The motion was tracked with the imaging detector, and the tip was moved back manually to the same location in the images. During temperature holding stage, the thermocouple was thermally equilibrated, so the tip did not move in the image field of view. This thermocouple position-adjustment procedure is also used in other sample experiments. Another K-type thermocouple (B) was inserted from the side of the heater, used for the closed-loop power feedback control. To calibrate the temperature offset, the sample position temperature was ramped from room temperature to 1100°C in 100°C increments. Fig. 2(c) shows the temperature offset difference between two thermocouples, as expected due to their different positions. The calibration was reproducible through multiple thermal cycles.

The temperature distribution within the sample heating zone was characterized over a 1 mm × 1 mm × 1 mm 3D grid, with 0.1 mm step size. The cooling and heating rates of the heater were also tested. The temperature distribution results in Fig. 2(d) show that the temperature distribution around the sample heating zone has gradients less than 5.7°C mm^{-1} in the transverse plane and 13.7°C mm^{-1} in the vertical direction. Within the microscope field-of-view region, which is about 30–50 μm for 30 nm spatial resolution at 8 keV, the temperature variation is therefore negligible in all directions for practical purposes. The results also show the heater has good temperature stability. In the test temperature range, the temperature fluctuated around the target temperature within ±1.6°C (standard deviation).

3. Applications

The furnace has been used in various *in situ* heating experiments conducted with the TXM at the FXI beamline of NSLS-II. Two example cases are presented here to demonstrate the capability.

3.1. 3D nano-tomography under a liquid molten salt extreme environment to study metal corrosion and dealloying

Molten salts are one of the leading candidates for high-temperature heat-transfer fluids and play a critical role in the development of future nuclear and solar energy (Misra & Whittenberger, 1987; Williams *et al.*, 2006; Sridharan *et al.*, 2012; Sohal *et al.*, 2010; Ruh & Spiegel, 2006; Raiman &

Lee, 2018). The ability to observe the morphological evolution of alloys in molten salt in real time to understand the behaviors and kinetics, while at the elevated temperatures, is a vital advancement. The results of an *in situ* study of the 3D morphological evolution with time of a Ni-20Cr wire in a molten 50:50 mol% MgCl$_2$:KCl salt mixture, sealed in an Ar-filled quartz capillary, are shown in Fig. 3 (for further details see Section S2 of the supporting information). Rapid morphological evolution caused by corrosion is seen from the pristine sample in Fig. 3(a) after only 16 min in the molten salt at 800°C [Fig. 3(b)]. This structure continues to corrode and forms a bicontinuous 3D network of pores by 33 min [Fig. 3(c)], analogous to the dealloying process which forms nano- and meso-porous structures for functional applications (Erlebacher *et al.*, 2001; Zhao *et al.*, 2017, 2019; Chen-Wiegart *et al.*, 2013). The corrosion process slows in 33–185 min [Figs. 3(c) and 3(d)] as the Cr has probably been depleted and Ni itself corrodes at a slower rate. At this later time point, structural coarsening is expected as surface diffusion drives changes in surface curvature to lower the overall free energy of the system. The result demonstrates the feasibility of studying materials evolution in molten salts or other extreme environments under *in situ* conditions.
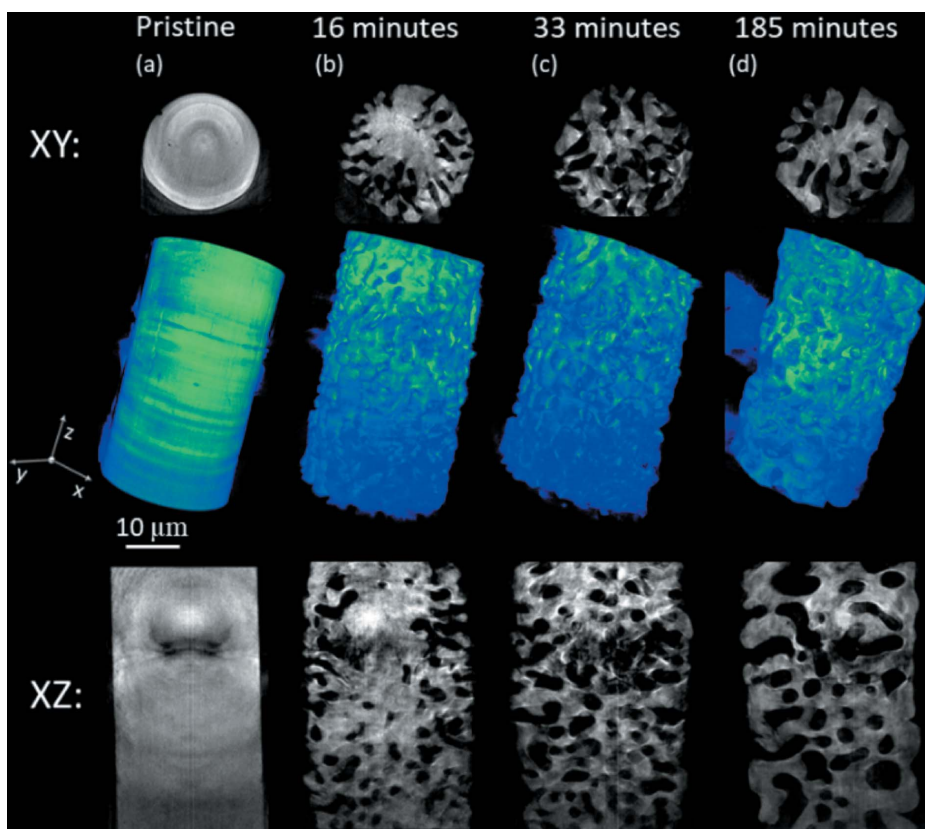

Figure 3
In situ study of Ni-20Cr wire in molten 50:50 mol% KCl:MgCl$_2$ at 800°C. Before heating, the pristine sample (a) is homogeneous and free of major defects. After only 16 min (b) at temperature, significant corrosion has taken place. After 33 min (c) corrosion has further progressed, resulting in a bi-continuous pore formation. After 185 min (d) surface coarsening drives the formation of elongated and smooth channels.

3.2. 3D nano-tomography at elevated temperature to study pore formation in icosahedral quasicrystals

Quasicrystals (QCs) are solids that exhibit long-range order but no periodicity. Since their discovery over 30 years ago (Shechtman *et al.*, 1984), a vast number of quasicrystal-forming alloys have been discovered from which single QCs with a high degree of structural perfection can be grown (Tsai *et al.*, 1987; Ritsch, 1996). Nevertheless, defects such as pores [so-called 'negative crystals' (Sunagawa, 1981)] are still present and are thought to be influenced by the peculiar properties of QCs. Two hypotheses have been proposed to explain the extended porosity in QCs, and particularly in the icosahedral Al–Pd–Mn phase. The first concerns the condensation of vacancies (Beeli *et al.*, 1998) and the second invokes a structure model which considers 'hierarchical porosity' as an intrinsic feature (Janot *et al.*, 1998).

To assess the validity of these hypotheses, we investigated the structural transformation of a melt-spun $Al_{70}Pd_{20}Mn_{10}$ alloy (in the form of a micropillar) during heat treatment. No inherent porosity was detected at the earliest stage of annealing; however, we observe the nucleation and growth of pores at the surface of the sample after 42 min of annealing. As the pores grow, they develop facets [Figs. 4(a) and 4(b)] fully consistent with the solid–vapor Wulff shape of QCs (Beeli *et al.*, 1998; Mancini *et al.*, 1998). Altogether these results point to the strong influence of vacancy diffusion on porosity formation. Pore formation requires a vacancy supersaturation **S** of thermal vacancies (Gastaldi *et al.*, 2006), which we calculate to be $S \gg 1$ (see Section S3 of the supporting information), assuming that all vacancies existing at the melting temperature (T_m) condense into pores below T_m. Vacancies may also be created during high-temperature

oxidation: the metal cations diffuse from the oxide/alloy interface into the oxide, leaving behind an equal number of vacancies. The vacancies then coalesce into voids beneath the oxide layer (Oleksak *et al.*, 2018). The behavior of these vacancies is not considered in conventional oxidation theory (Wagner, 1933), which assumes that they are constantly annihilated at the oxide/alloy interface (Gibbs & Hales, 1977). The observation of multiple pores on the external surfaces *via* scanning electon microscopy (SEM) [Fig. 4(c)] further supports this idea.

4. Conclusions

A compact *in situ* heater has been designed, fabricated and commissioned at NSLS-II. The module demonstrated a high level of stability for targeted TXM imaging experiments. The excellent performance, simplicity and versatility of its design make this heater suitable for use in a broad range of scientific applications in materials research and beyond. We should point out that the design presented here is targeted specifically at TXM applications. The field of view in TXM experiments is small (<50 μm) so a temperature gradient up to $10^{\circ}C\,mm^{-1}$ would be acceptable. To work with a larger sample and field of view, it would be necessary to scale up the furnace size to provide a larger uniform hot zone. Furthermore, the small furnace chamber space in the present TXM setup makes it difficult to integrate other types of sample environment controls into the furnace itself. However, it is possible to integrate certain controls into the sample holder design. For instance, it is possible to design a sample holder to include a quartz capillary to flow gas through sample during an experiment. Nonetheless, the current furnace design demonstrates an approach that provides precise heat management at the sample position and in the ambient environment around the sample. Modifications to this basic design could lead to a customized furnace design that is suitable for versatile tasks that address user-specific experimental requirements.

5. Related literature

The following references are cited in the supporting information: Dovbenko *et al.* (2005); Dowd *et al.* (1999); Gursoy *et al.* (2014); Rivers (2012); Sato *et al.* (2003).
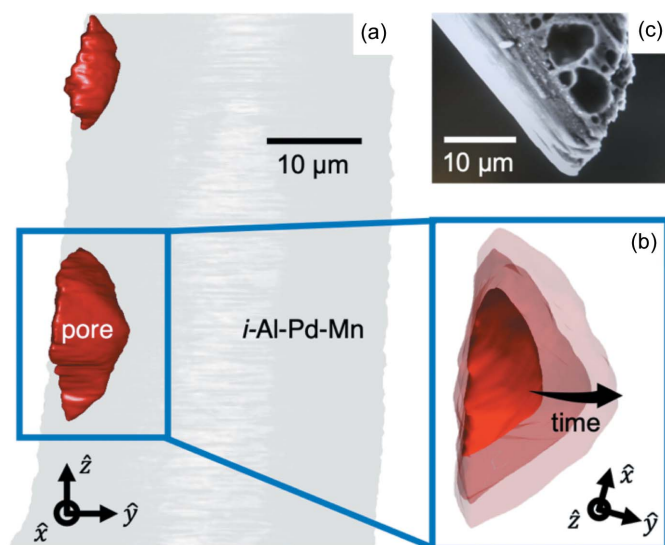
Figure 4
(*a*) 3D reconstruction of pores (red) grown from the Al–Pd–Mn QC matrix (gray) after 60 min at 800°C. (*b*) Bird's-eye view of pore growth, showing interfacial isochrones at three consecutive time-steps (51, 60 and 69 min). (*c*) Evaluation of the sample surface using SEM after annealing for 2 h at 800°C. The darker features are pores.

rapid 3D tomography data George R. Lindemann and Paul Chao. The authors thank: Phillip Halstenberg, Shannon M. Mahurin and Sheng Dai of Oak Ridge National Laboratory for the purified salt mixture.

References

Bale, H. A., Haboub, A., MacDowell, A. A., Nasiatka, J. R., Parkinson, D. Y., Cox, B. N., Marshall, D. B. & Ritchie, R. O. (2013). *Nat. Mater.* **12**, 40–46.

Barnard, H. S., MacDowell, A. A., Parkinson, D. Y., Mandal, P., Czabaj, M., Gao, Y., Maillet, E., Blank, B., Larson, N. M., Ritchie, R. O., Gludovatz, B., Acevedo, C. & Liu, D. (2017). *J. Phys. Conf. Ser.* **849**, 012043.

Beeli, C., Godecke, T. & Luck, R. (1998). *Philos. Mag. Lett.* **78**, 339–348.

Cheng, J. H., Assegie, A. A., Huang, C. J., Lin, M. H., Tripathi, A. M., Wang, C. C., Tang, M. T., Song, Y. F., Su, W. N. & Hwang, B. J. (2017). *J. Phys. Chem. C*, **121**, 7761–7766.

Chen-Wiegart, Y. K., Harris, W. M., Lombardo, J. J., Chiu, W. K. S. & Wang, J. (2012). *Appl. Phys. Lett.* **101**, 253901.

Chen-Wiegart, Y. K., Wada, T., Butakov, N., Xiao, X. H., De Carlo, F., Kato, H., Wang, J., Dunand, D. C. & Maire, E. (2013). *J. Mater. Res.* **28**, 2444–2452.

Chen-Wiegart, Y. K., Wang, S., Chu, Y. S., Liu, W. J., McNulty, I., Voorhees, P. W. & Dunand, D. C. (2012). *Acta Mater.* **60**, 4972–4981.

Dovbenko, O., Velikanova, T. & Balanetskyy, S. (2005). *Ternary Alloy Systems. Phase Diagrams, Crystallographic and Thermodynamic Data. Group IV: Physical Chemistry.* Subvolume A. MSIT Publishing.

Dowd, B. A., Campbell, G. H., Marr, R. B., Nagarkar, V., Tipnis, S., Axe, L. & Siddons, D. P. (1999). *Proc. SPIE*, **3772**, 224–236.

Erlebacher, J., Aziz, M. J., Karma, A., Dimitrov, N. & Sieradzki, K. (2001). *Nature*, **410**, 450–453.

Fife, J. L., Rappaz, M., Pistone, M., Celcer, T., Mikuljan, G. & Stampanoni, M. (2012). *J. Synchrotron Rad.* **19**, 352–358.

Gastaldi, J., Schenk, T., Reinhart, G., Klein, H., Härtwig, J., Mangelinck-Noël, N., Grushko, B., Nguyen Thi, H., Pino, P., Billia, B. & Baruchel, J. (2006). *Philos. Mag.* **86**, 335–340.

Gatalo, M., Ruiz-Zepeda, F., Hodnik, N., Dražić, G., Bele, M. & Gaberšček, M. (2019). *Nano Energy*, **63**, 103892.

Ge, M., Coburn, D. S., Nazaretski, E., Xu, W., Gofron, K., Xu, H., Yin, Z. & Lee, W.-K. (2018). *Appl. Phys. Lett.* **113**, 083109.

Gibbs, G. & Hales, R. (1977). *Corros. Sci.* **17**, 487–507.

Gibbs, J. W., Mohan, K. A., Gulsoy, E. B., Shahani, A. J., Xiao, X., Bouman, C. A., De Graef, M. & Voorhees, P. W. (2015). *Sci. Rep.* **5**, 11824.

Gonzalez-Jimenez, I. D., Cats, K., Davidian, T., Ruitenbeek, M., Meirer, F., Liu, Y. J., Nelson, J., Andrews, J. C., Pianetta, P., de Groot, F. M. F. & Weckhuysen, B. M. (2012). *Angew. Chem. Int. Ed.* **51**, 11986–11990.

Gürsoy, D., De Carlo, F., Xiao, X. & Jacobsen, C. (2014). *J. Synchrotron Rad.* **21**, 1188–1193.

Han, I., Xiao, X., Sun, H. & Shahani, A. J. (2019). *Acta Cryst.* A**75**, 281–296.

Harris, W. M., Lombardo, J. J., Nelson, G. J., Lai, B., Wang, S., Vila-Comamala, J., Liu, M., Liu, M. & Chiu, W. K. S. (2015). *Sci. Rep.* **4**, 5246.

Izzo, J. R., Joshi, A. S., Grew, K. N., Chiu, W. K. S., Tkachuk, A., Wang, S. H. & Yun, W. B. (2008). *J. Electrochem. Soc.* **155**, B504–B508.

Janot, C., Loreto, L., Farinato, R., Mancini, L., Baruchel, J. & Gastaldi, J. (1998). *Mater. Res. Soc. Symp. Proc. Ser.* **553**, 55–66.

Johnson, K. J., Wiegart, L., Abbott, A. C., Johnson, E. B., Baur, J. W. & Koerner, H. (2019). *Langmuir*, **35**, 8758–8768.

Kaira, C. S., Stannard, T. J., De Andrade, V., De Carlo, F. & Chawla, N. (2019). *Acta Mater.* **176**, 242–249.

Kiss, A. M., Harris, W. M., Nakajo, A., Wang, S., Vila-Comamala, J., Deriy, A. & Chiu, W. K. S. (2015). *Microsc. Microanal.* **21**, 290–297.

Landa-Medrano, I., Sorrentino, A., Stievano, L., de Larramendi, I. R., Pereiro, E., Lezama, L., Rojo, T. & Tonti, D. (2017). *Nano Energy*, **37**, 224–231.

Li, L., Chen-Wiegart, Y. K., Wang, J., Gao, P., Ding, Q., Yu, Y.-S., Wang, F., Cabana, J., Wang, J. & Jin, S. (2015). *Nat. Commun.* **6**, 6883.

Liu, X., Vonk, D., Jiang, H., Kisslinger, K., Tong, X., Ge, M., Nazaretski, E., Ravel, B., Foster, K., Petrash, S. & Chen-Wiegart, Y. K. (2019). *ACS Appl. Nano Mater.* **2**, 1920–1929.

Mancini, L., Janot, C., Loreto, L., Farinato, R., Gastaldi, J. & Baruchel, J. (1998). *Philos. Mag. Lett.* **78**, 159–167.

Mao, W. L., Lin, Y., Liu, Y. J. & Liu, J. (2019). *Engineering*, **5**, 479–489.

Milhet, X., Nait-Ali, A., Tandiang, D., Liu, Y. J., Van Campen, D., Caccuri, V. & Legros, M. (2018). *Acta Mater.* **156**, 310–317.

Misra, A. K. & Whittenberger, J. D. (1987). *Proceedings of 22nd Intersociety Energy Conversion Engineering Conference (IECEC)*, 10–14 August, 1987, Philadelphia, PA, p. 9226. American Institute of Aeronautics and Astronautics.

Moniri, S., Xiao, X. & Shahani, A. J. (2019). *Sci. Rep.* **9**, 3381.

Oleksak, R. P., Kapoor, M., Perea, D. E., Holcomb, G. R. & Doğan, Ö. N. (2018). *npj Mater. Degrad.* **2**, 25.

Raiman, S. S. & Lee, S. (2018). *J. Nucl. Mater.* **511**, 523–535.

Ritsch, S. (1996). *Philos. Mag. Lett.* **74**, 99–106.

Rivers, M. L. (2012). *Proc. SPIE*, **8506**, 850628.

Ruh, A. & Spiegel, M. (2006). *Corros. Sci.* **48**, 679–695.

Sato, K., Baier, F., Rempel, A. A., Sprengel, W. & Schaefer, H. E. (2003). *Phys. Rev. B*, **68**, 214203.

Shahani, A. J., Xiao, X. & Voorhees, P. W. (2016). *Nat. Commun.* **7**, 12953.

Shechtman, D., Blech, I., Gratias, D. & Cahn, J. W. (1984). *Phys. Rev. Lett.* **53**, 1951–1953.

Sohal, M. S., Ebner, M. A., Sabharwall, P. & Sharpe, P. (2010). *Engineering Database of Liquid Salt Thermophysical and Thermochemical Properties*, https://www.osti.gov/biblio/980801-engineering-database-liquid-salt-thermophysical-thermochemical-properties.

Sridharan, K., Allen, T., Anderson, M. & Simpson, M. (2012). *Thermal Properties of LiCl-KCl Molten Salt for Nuclear Waste Separation Idaho Falls*. Technical Report. University of Wisconsin,

Madison, WI, USA; Idaho National Laboratory, ID, USA (https://www.osti.gov/servlets/purl/1058922/).

Sunagawa, I. (1981). *Bull. Minéral.* **104**, 81–87.

Topsøe, H. (2003). *J. Catal.* **216**, 155–164.

Tsai, A. P., Inoue, A. & Masumoto, T. (1987). *Jpn. J. Appl. Phys.* **26**, L1994–L1996.

Tsai, P. C., Wen, B. H., Wolfman, M., Choe, M. J., Pan, M. S., Su, L., Thornton, K., Cabana, J. & Chiang, Y. M. (2018). *Energy Environ. Sci.* **11**, 860–871.

Voorhees, P. W. (1985). *J. Stat. Phys.* **38**, 231–252.

Wagner, C. (1933). *Z. Phys. Chem.* **21**, 25–41.

Waldmann, T., Wilka, M., Kasper, M., Fleischhammer, M. & Wohlfahrt-Mehrens, M. (2014). *J. Power Sources*, **262**, 129–135.

Williams, D., Toth, L. & Clarno, K. (2006). Technical Report ORNL/TM-2006/12. Oak Ridge National Laboratory, TN, USA (https://info.ornl.gov/sites/publications/Files/Pub57476.pdf).

Xu, Y. H., Hu, E. Y., Zhan, K., Wang, X. L., Borzenets, V., Sun, Z. H., Pianetta, P., Yu, X. Q., Liu, Y. J., Yang, X. Q. & Li, H. (2017). *ACS Energy Lett.* **2**, 1240–1245.

Yang, Y., Xu, R., Zhang, K., Lee, S., Mu, L., Liu, P., Waters, C. K., Spence, S., Xu, Z., Wei, C., Kautz, D. J., Yuan, Q., Dong, Y., Yu, Y., Xiao, X., Lee, H., Pianetta, P., Cloetens, P., Lee, J., Zhao, K., Lin, F. & Liu, Y. (2019). *Adv. Energy Mater.* **9**, 1900674.

Zhao, C., Wada, T., De Andrade, V., Gürsoy, D., Kato, H. & Chen-Wiegart, Y. K. (2018). *Nano Energy*, **52**, 381–390.

Zhao, C. H., Kisslinger, K., Huang, X. J., Lu, M., Camino, F., Lin, C. H., Yan, H. F., Nazaretski, E., Chu, Y., Ravel, B., Liu, M. Z. & Chen-Wiegart, Y. K. (2019). *Mater. Horiz.* **6**, 1991–2002.

Zhao, C. H., Wada, T., De Andrade, V., Williams, G. J., Gelb, J., Li, L., Thieme, J., Kato, H. & Chen-Wiegart, Y. K. (2017). *Appl. Mater. Interfaces*, **9**, 34172–34184.